



**HAL**  
open science

## Tubular optical microcavities based on rolled-up photonic crystals

Rémi Briche, Aziz Benamrouche, Pierre Cremillieu, Philippe Regreny, Jean-Louis Leclercq, Xavier Letartre, Alexandre Danescu, Ségolène Callard

► **To cite this version:**

Rémi Briche, Aziz Benamrouche, Pierre Cremillieu, Philippe Regreny, Jean-Louis Leclercq, et al.. Tubular optical microcavities based on rolled-up photonic crystals. *APL Photonics*, 2020, 5 (10), pp.106106. 10.1063/5.0022862 . hal-02975203

**HAL Id: hal-02975203**

**<https://hal.science/hal-02975203>**

Submitted on 22 Nov 2021

**HAL** is a multi-disciplinary open access archive for the deposit and dissemination of scientific research documents, whether they are published or not. The documents may come from teaching and research institutions in France or abroad, or from public or private research centers.

L'archive ouverte pluridisciplinaire **HAL**, est destinée au dépôt et à la diffusion de documents scientifiques de niveau recherche, publiés ou non, émanant des établissements d'enseignement et de recherche français ou étrangers, des laboratoires publics ou privés.

# Tubular optical microcavities based on rolled-up photonic crystals <sup>EP</sup>

Cite as: APL Photonics 5, 106106 (2020); <https://doi.org/10.1063/5.0022862>

Submitted: 24 July 2020 . Accepted: 28 September 2020 . Published Online: 12 October 2020

 Rémi Briche, Aziz Benamrouche, Pierre Cremillieu, Philippe Regreny,  Jean-Louis Leclercq, Xavier Letartre, Alexandre Danescu, and  Ségolène Callard

## COLLECTIONS

 This paper was selected as an Editor's Pick



View Online



Export Citation



CrossMark

## ARTICLES YOU MAY BE INTERESTED IN

[Silicon nitride chirped spiral Bragg grating with large group delay](#)

APL Photonics 5, 101302 (2020); <https://doi.org/10.1063/5.0022963>


[Perfectly absorbing dielectric metasurfaces for photodetection](#)

APL Photonics 5, 101304 (2020); <https://doi.org/10.1063/5.0019883>

[Low-loss low thermo-optic coefficient Ta<sub>2</sub>O<sub>5</sub> on crystal quartz planar optical waveguides](#)

APL Photonics 5, 116103 (2020); <https://doi.org/10.1063/5.0024743>

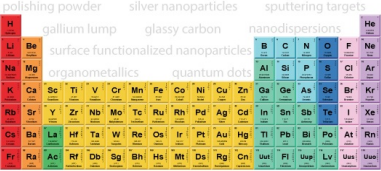
additive manufacturing epitaxial crystal growth cerium oxide polishing powder silver nanoparticles sputtering targets



THE ADVANCED MATERIALS MANUFACTURER®

deposition slugs OLED Lighting spintronics solar energy osmium nanoribbons thin films chalcogenides AuNPs GDC Li-ion battery electrolytes 99.999% ruthenium spheres

endohedral fullerenes copper nanoparticles diamond micropowder CIGS MBE grade materials palladium catalysts flexible electronics beta-barium borate borosilicate glass dysprosium pellets YBCO pyrolytic graphite 3d graphene foam indium tin oxide mesoporous silica raman substrates sapphire windows tungsten carbide InGaAs barium fluoride carbon nanotubes lithium niobate scandium powder



gallium lump glassy carbon nanodispersions III-IV semiconductors CVD precursors europium phosphors InAs wafers laser crystals ultra high purity materials MOFs rare earth metals photovoltaics refractory metals MOCVD superconductors transparent ceramics ultra high purity silicon

organometallics quantum dot

American Elements opens up a world of possibilities so you can **Now Invent!**

Over 15,000 certified high purity laboratory chemicals, metals, & advanced materials and a state-of-the-art Research Center. Printable GHS-compliant Safety Data Sheets. Thousands of new products. And much more. All on a secure multi-language 'Mobile Responsive' platform.

perovskite crystals yttrium iron garnet alternative energy h-BN gold nanocubes graphene oxide macromolecules photonics rhodium sponge fiber optics beamsplitters infrared dyes zeolites fused quartz metallocenes platinum ink buckyballs Ti-6Al-4V

**Now Invent.™**  
The Next Generation of Material Science Catalogs

[www.americanelements.com](http://www.americanelements.com)

# Tubular optical microcavities based on rolled-up photonic crystals

Cite as: APL Photon. 5, 106106 (2020); doi: 10.1063/5.0022862

Submitted: 24 July 2020 • Accepted: 28 September 2020 •

Published Online: 12 October 2020



View Online



Export Citation



CrossMark

Rémi Briche,<sup>a)</sup>  Aziz Benamrouche, Pierre Cremillieu, Philippe Regreny, Jean-Louis Leclercq,  Xavier Letartre, Alexandre Danescu, and Ségolène Callard 

## AFFILIATIONS

Université de Lyon, École Centrale de Lyon, Institut des Nanotechnologies de Lyon, CNRS, UMR5270, Lyon, France

<sup>a)</sup> Author to whom correspondence should be addressed: [remi.briche@ec-lyon.fr](mailto:remi.briche@ec-lyon.fr)

## ABSTRACT

The self-rolling of micro-structured membranes via the stress-engineering method opens new ways to create 3D photonic micro-objects with original designs and optical properties. This article validates this approach by producing 3D hollow micro-resonators based on rolled-up 2D photonic crystal membrane mirrors, capable of trapping light in 3D and in air. We fabricated the 3D tubular microresonators with 10  $\mu\text{m}$ –20  $\mu\text{m}$  diameters by rolling photonic crystal membranes using stress-engineering technique on the prestressed InGaP/InP bilayer. We also added a design feature to lift the microtubes vertically and facilitate optical measurements, but also to attach the structures to the substrate. The dispersion of the planar 2D photonic crystal membrane was optimized to exhibit high reflectivity (>95%) at normal incidence over a large spectral band (100 nm) in the near-infrared domain (1.5  $\mu\text{m}$ –1.6  $\mu\text{m}$ ). The cylindrical cavity model and numerical simulations predicted the presence of quasi-pure radial cavity modes with a strong concentration of light over nearly 3% of the photonic microtubes' cross section. We demonstrated experimentally the presence of those modes through scanning near-field optical microscopy measurements. Using a bowtie nanoantenna, we selectively detected and mapped transverse electric modes in the hollow core of photonic microtubes. Spatially resolved cartographies allowed for the identification of the modes in good agreement with theoretical predictions. This work brings theoretical and experimental proof of concept of light cages based on rolled-up photonic crystal membranes. It also opens the path to the realization of original photonic microstructures as combinations of a specific photonic crystal design and a targeted 3D form.

© 2020 Author(s). All article content, except where otherwise noted, is licensed under a Creative Commons Attribution (CC BY) license (<http://creativecommons.org/licenses/by/4.0/>). <https://doi.org/10.1063/5.0022862>

## I. INTRODUCTION

Since the pioneer works of Prinz,<sup>1,2</sup> nanofabrication techniques based on self-rolling of pre-stressed membranes have been developed in a thriving way toward the production of 3D microstructures with unconventional geometries such as tubes,<sup>3</sup> coils,<sup>4</sup> or even Origami-based nano-objects,<sup>5–9</sup> accessible with a large range of materials. Based on the stress-engineering method, a high degree of control over the size and geometry of the structures can be achieved, making them suitable in a wide range of applications related to electronics,<sup>10</sup> nanomachines,<sup>11</sup> energy harvesting,<sup>12</sup> or biology.<sup>13</sup> Among the variety of 3D architectures, rolled-up tubular microcavities have, for instance, drawn great interest for optofluidic applications by combining their microchannel geometry and

particular optical properties of the tube to produce highly sensitive fluid sensors.<sup>14–16</sup> In addition, very low threshold lasers<sup>17,18</sup> have been developed by exploiting high quality whispering gallery modes (WGMs) generated in the optically active membrane wall of the microtube. However, applying the stress-engineering method to fold more complex surfaces such as photonic nanostructured membranes opens new ways to produce 3D photonic micro-objects with original designs and optical properties. Indeed, the structuration provides additional degrees of freedom with the modification of the dispersion of the planar membrane, which enables various optical functionalities such as the guiding, the trapping, or the slowing of light. The rolling of a 2D photonic crystal membrane (PCM) has, for instance, been discussed theoretically<sup>19,28</sup> to produce 3D photonic crystals (PCs), which exhibit a full photonic bandgap. Therefore,

the combination between the variety of optical properties available with PCM and 3D rolled-up designs offers new strategies for the management of light.

In particular, the use of the PCM has been proposed to form photon cages. Those structures are based on the deformation of a highly reflective PCM<sup>20</sup> so as to form 3D hollow micro-resonators. In photon cages, the reflecting walls allow to trap efficiently the light in the hollow core of the cavity, in air or in a low index medium. Consequently, it optimizes the overlap between the localized electromagnetic field and a surrounding medium, a keystone in sensing operations. Indeed, with a proper design, a 1D high-index-contrast PCM<sup>21</sup> can be used as broadband, non-absorbing mirrors, more compact than traditional Bragg mirrors.<sup>22</sup> High reflectivity is obtained by optimizing the coupling between the incident radiating light and the PCM slow light  $\Gamma$ -modes.<sup>23</sup> Hence, a cylindrical arrangement of Si pillars regularly spaced to reproduce the PCM parameters can form a cylindrical resonator in which the electromagnetic field could be efficiently trapped in the inner part of the cylinder.<sup>24</sup> However, from a practical point of view, these structures are demanding in terms of fabrication as they require pillars with a very high aspect ratio (1:20). Moreover, in the 1D PCM, the reflectivity is strongly dependent on the polarization of the field, and consequently, the mirror properties are only efficient for one specific polarization. This drawback can be avoided with 2D PCM mirrors.

In the present article, we show that the rolled-up nanotechnology offers an interesting platform to implement the photon cage concept in an original geometry. Here, we present a novel fabrication technique of the rolled-up 2D PCM to form tubular photon cages. By performing optical characterizations, we validate the approach with the demonstration of the presence of optical cylindrical cavity modes in air. Those results open new horizons for the creation of original 3D photonic micro-objects based on other combinations of 2D PCM designs and properties and 3D targeted forms.

This paper is organized as follows: Sec. I focuses on the design of the PCM to make an efficient and broadband mirror in the near-infrared domain by adjusting the parameters of the 2D photonic crystal. The reflecting power of the PCM is assessed numerically at normal and oblique incidence. Sec. II presents the design and the fabrication of the rolled-up photonic crystal membrane. The curvature radii of the photonic microtubes obtained by stress relaxation of a pre-stressed semiconductor bilayer are calculated by using a classical expression derived from linear plate theory. Sec. III introduces the analytical and numerical tools used to predict the optical response of the final rolled-up structure. The analytical model of the cylindrical cavity resonator provides preliminary estimates of the optical properties of the photonic microtubes. Finite-difference time-domain (FDTD) computations complete those predictions with more realistic results in agreement with the properties of the real structures. In Sec. IV, we describe the scanning near-field optical microscopy (SNOM) setup used to characterize optically the fabricated tubular cavities. Electric field intensity maps of the modes supported by the photonic microtubes and obtained after SNOM scans are then discussed. Those results bring experimental evidence of the existence of cylindrical cavity modes in the rolled-up PCM in agreement with spectral and spatial distributions of the modes predicted by analytic and numerical computations.

## II. DESIGN OF THE PLANAR 2D PHOTONIC CRYSTAL MEMBRANE MIRROR

A planar 2D photonic crystal membrane (PCM) was first designed to produce a broadband mirror in the near-infrared domain. The pattern of the photonic crystal consisted of a triangular lattice (period  $a$ ) of air holes (radius  $r$ ) inside a semi-conducting indium phosphide (InP with  $n_{\text{InP}} \approx 3.16$  at  $1.55 \mu\text{m}$ ) slab, as depicted in Fig. 1(a). The reflectivity  $R(\lambda)$  of the PCM with the infinite lateral size was calculated at normal incidence using the Rigorous Coupled-Wave Analysis (RCWA) method over the spectral window  $[1.4\text{--}1.8] \mu\text{m}$ . Parameters of the photonic crystal were optimized, taking into account fabrication constraints (see Sec. III), to achieve a high and broadband reflecting behavior around  $1.6 \mu\text{m}$ . Therefore, with  $a = 1.206 \mu\text{m}$ ,  $r = 0.480 \mu\text{m}$ , and  $h = 0.230 \mu\text{m}$ , the reflectivity of the PCM  $R(\lambda)$  lies above 95% over a 100 nm-large spectral range, as shown in Fig. 1(b). Unlike the 1D PCM,<sup>24</sup> we notice that reflection properties of the 2D PCM at normal incidence are independent of the orientation of the electric field  $\vec{E}$  in the plane of the PC membrane. We also compared the reflection properties at normal incidence of the PCM to those of an ordinary gold mirror derived from Fresnel reflection coefficients. Figure 1(b) shows that both reflecting powers are competitive in the spectral range  $[1.5\text{--}1.7] \mu\text{m}$ . The reflectivity of the PCM is even higher between  $1.56 \mu\text{m}$  and  $1.61 \mu\text{m}$ , reaching about 99% at  $1.59 \mu\text{m}$ . Despite excellent and broadband reflection properties, gold suffers from optical losses, hence limiting its reflectivity, whereas the InP material is transparent in the near-infrared domain. The reflectivity at normal incidence of an equivalent non-structured InP membrane was also estimated to assess the added-value of the structuration of the PCM. Between  $1.4 \mu\text{m}$  and  $1.8 \mu\text{m}$ , the InP membrane exhibits a low reflectivity, which remains below 50%, as shown in Fig. 1(b), with a minimum close to  $1.45 \mu\text{m}$  where the conditions for destructive interferences are also satisfied. Indeed, the mirror-like behavior of the PCM is all the more striking as it is obtained with a structure mostly filled with air (air filling factor of about 57%).

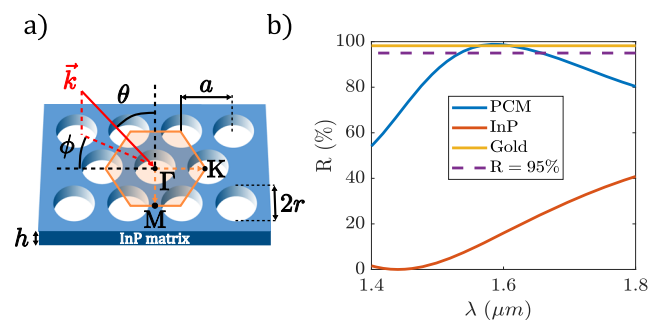


**FIG. 1.** (a) Scalable schematics of the 2D photonic crystal membrane (PCM): triangular lattice (period  $a$ ) of air holes (radius  $r$ ) in a semiconducting indium phosphide (InP) (refractive index  $n_{\text{InP}} \approx 3.16$  at  $1.55 \mu\text{m}$ ) membrane of thickness  $h$ . The orange contour delimits the Brillouin zone with high symmetry directions  $\Gamma\text{K}$  and  $\Gamma\text{M}$ . (b) Reflectivity spectra  $R(\lambda)$  of  $0.230 \mu\text{m}$ -thick membranes at normal incidence ( $\theta = 0$ ): PCM (blue) reflectivity computed with RCWA simulations and reflectivity of suspended non-structured InP (red) and gold (yellow) membranes derived from Fresnel reflection coefficients. The purple dashed line indicates the 95% high reflectivity limit.

Previous results about the reflection properties of the PCM are only valid at normal incidence. To assess their robustness in the case of oblique incidence, the reflectivity of the PCM was computed for increasing values of the angle of incidence  $\theta$  and for p-polarization and s-polarization. For p-polarized (s-polarized) light, the electric field  $\vec{E}$  is contained in (orthogonal to) the plane of incidence, as depicted in Fig. 2(a) and Fig. 2(b). The incident radiation points in the  $\Gamma\text{M}$  direction ( $\phi = \pi/2$ ) with respect to experimental conditions. For small variations of  $\theta$  up to  $10^\circ$  and p-polarized light, high reflectivity of the PCM ( $R > 95\%$ ) is maintained between  $1.57 \mu\text{m}$  and  $1.67 \mu\text{m}$ , as shown in Fig. 2(c). This proves the robustness of the mirror-like behavior over the spectral window of interest, between  $1.5 \mu\text{m}$  and  $1.6 \mu\text{m}$ . For s-polarized light, this robustness covers smaller deviations up to few degrees, as illustrated in Fig. 2(f). We noticed that similar results were obtained for the incident direction parallel to the  $\Gamma\text{K}$  direction ( $\phi = 0$ ). However, high reflecting power of the PCM holds for a planar membrane. In rolled-up structures, the induced curvature of the PCM might alter the reflection properties of the membrane optimized in the planar configuration. Curvature effects on reflection properties will be taken into account in FDTD simulations.

### III. DESIGN AND FABRICATION OF THE ROLLED-UP STRUCTURE

To roll the PCM mirror into a photonic microtube, we use stress engineering and start with a simple bilayer structure

InGaP/InP in which the amount of prestress is determined by the concentration of the gallium element in the upper layer. When the prestress is released (by the under-etching process), the bilayer adopts a natural curvature predicted by the following formula derived from the classical Love–Kirchhoff plate theory:<sup>6</sup>

$$\frac{1}{\rho} = \frac{6m\xi}{h_{\text{InP}}(1 + \xi)^3} \quad (1)$$

where  $\rho$  denotes the curvature radius of the final structure,  $m = (a_{\text{InP}} - a_{\text{InGaP}})/a_{\text{InGaP}}$  is the lattice mismatch with  $a_{\text{InP}}$  and  $a_{\text{InGaP}}$ , the lattice parameters of InP and InGaP materials, respectively, and  $\xi = h_{\text{InGaP}}/h_{\text{InP}}$ , where  $h_{\text{InGaP}}$  and  $h_{\text{InP}}$  denote the thicknesses of the InGaP and InP layers, respectively.

The lattice parameter  $a_{\text{InGaP}}$  varies with the composition in the gallium element  $x$  as  $a_{\text{InGaP}} = xa_{\text{GaP}} + (1 - x)a_{\text{InP}}$ . We define  $h$  as the total thickness of the bilayer InP/InGaP:  $h = h_{\text{InGaP}} + h_{\text{InP}}$ . According to Eq. (1), the value of the curvature radius can be tuned theoretically by varying the thicknesses of the two layers and the composition in the gallium element  $x$  in the InGaP layer. Indeed, the radius increases when increasing thicknesses of both layers. However, for a given mismatch  $m$ , the strain relaxation during the layer by layer (2D) epitaxial growth limits the thickness of the defect free InGaP layer. A compromise on the value of  $h$  has also to be found so as to meet optical requirements. In the following remarks, note that the InGaP/InP bilayer is considered to be equivalent to an InP membrane of thickness  $h$  as the refractive index of  $\text{In}_{(1-x)}\text{Ga}_x\text{P}$  is similar to that of InP

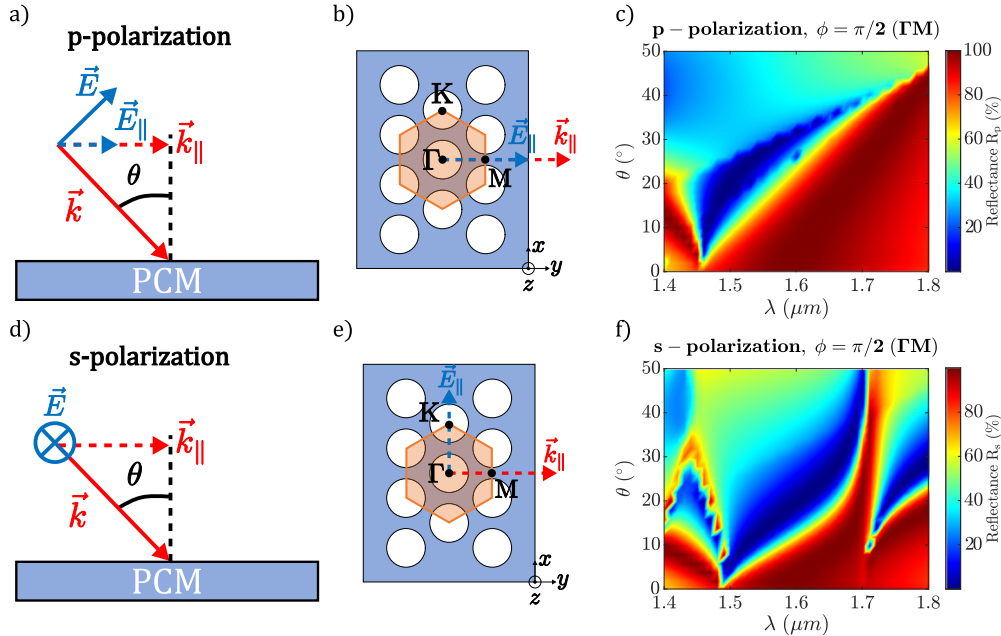


**FIG. 2.** Reflection properties of the PCM at oblique incidence  $\theta$ . Drawings (a) and (d): the polarization of the incident light (wavevector  $\vec{k}$ ) can decompose into the basis of p-polarization and s-polarization. Drawings (b) and (e): projections of the electric field  $\vec{E}_{\parallel}$  and the wavevector  $\vec{k}_{\parallel}$  onto the PCM for p-polarization and s-polarization, respectively, along high symmetry points of the first Brillouin zone (orange contour) of the PC lattice  $\Gamma$ , K, and M. The orientation of the photonic crystal, with respect to the experimental configuration, is such that  $\phi = \pi/2$ . Graphs (c) and (f): reflectivity of the PCM (RCWA simulations) for each polarization as a function of the angle of incidence  $\theta$ .

in the near-infrared for small  $x$  values. Therefore, the increasing total thickness  $h$  allows high orders of the slab to coexist, which can be an advantage as it favors the likelihood of two modes with large bandwidths to combine and produce broadband reflection of the PCM. However, increasing  $h$  implies a larger curvature radius and larger microtubes are most likely to support a considerable number of cavity modes.

The fabrication processes of the photonic microtubes are completely described in Refs. 6 and 8. We insist that the shape of the planar mask and the stress distribution require special care as they determine the 3D geometry of the final object. Figure 3(a) shows a scanning electron microscopy (SEM) picture of the mask pattern, which includes the PCM obtained after the e-beam lithography process with a closer view on the photonic crystal lattice. The green zone delimits the exposition area, which extends around the photonic crystal pattern to facilitate the under-etching process. The length of the PCM determines the number of rolls made by the membrane for a given curvature radius  $\rho$ : here, we set it to  $2\pi\rho$ , namely, the circumference of the tube, to achieve only one rolling. The under-etching step releases intrinsic stresses in the PCM following the blue dashed arrow drawn in Fig. 3(a) and triggers the self-rolling of the PCM into a horizontal cylindrical form. At the level of the specifically designed strip (yellow band), the rolled-up PCM starts to flip vertically. We stop the under-etching process at the end of the strip to anchor the structures to the substrate, as shown in Fig. 3(b). The vertical lifting operation allows us to make the inside of the microtube accessible to near-field probes and to manage the exploration of the modes of the microtube via scanning near-field optical microscopy (SNOM) measurements. In practice, for  $x \in [0.10-0.15]$  and  $h \in [100-230]$  nm, the measured curvature radius ranges from  $10 \mu\text{m}$  to  $20 \mu\text{m}$ . It is noteworthy that  $\rho \gg a (=1.206 \mu\text{m})$ ; hence, it is expected that curvature effects will have little impact on the reflection properties of the planar PCM mirror. However, as mentioned previously, we also expect a large number of modes to be supported by the photonic microtube.

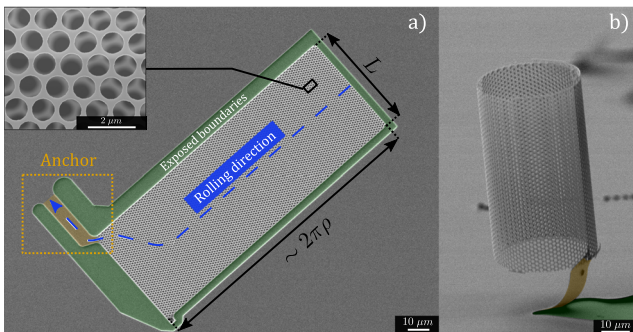


**FIG. 3.** (a) SEM picture of the planar design of the 2D photonic crystal membrane before rolling by the under-etching procedure. The inset picture zooms in on the photonic crystal lattice. The green zone covers parts of the e-beam lithography exposition area. The blue dashed arrow indicates the direction of under-etching, which triggers the rolling and the vertical lifting of the microtube via the specifically designed strip (anchor zone in yellow). (b) SEM picture of the final photonic microtube after rolling and vertical lifting of the photonic crystal membrane.

## IV. MODELING OPTICAL RESPONSE OF PHOTONIC MICROTUBES

### A. Analytical cylindrical cavity model

To predict the optical response of the rolled-up PCM, we used the well-known model of cylindrical cavity resonators. Assuming that the wall of the photonic microtube behaves as a perfect mirror, this model represents a simple and quick method to assess the number of modes hosted by the photonic microtube and to calculate their spectral and spatial distributions, as detailed in Ref. 25. Infinitely long cylindrical cavities host two kinds of modes:  $TE_{m,n}$  and  $TM_{m,n}$  modes described by  $m$  (azimuthal) and  $n$  (radial) orders and defined by  $E_z = 0$  and  $H_z = 0$ , respectively. We focus thereafter on  $TE_{m,n}$  modes. Note that when the cylindrical cavity has a finite length  $L$  and reflecting boundaries, order  $p$  of the  $TE_{m,n,p}$  mode accounts for the quantification of the wavevector along the cavity axis. Regarding the photonic structures, the vertical confinement of light is ensured by impedance mismatch between the inside and the outside of the photonic microtube.<sup>24</sup>

We estimated then the number of modes supported by a cylindrical cavity resonator with the fixed radius  $\rho$  and height  $L$  (see the inset of Fig. 4) within a specific spectral window. Figure 4(b) presents the evolution of the number of TE modes in the wavelength range  $[1.4-1.8] \mu\text{m}$  as a function of the cavity radius  $\rho$  for infinitely long tubes (blue dots) and  $50 \mu\text{m}$ -long tubes (red stars). With  $\rho = 17.5 \mu\text{m}$  (typical radius of fabricated structures), the number of TE modes reaches 311 for infinitely long cylinders and 6241 for  $50 \mu\text{m}$ -long tubes due to the quantization along the cavity axis.

Among the variety of  $TE_{m,n,p}$  modes that can be supported by the cavity, the modes with low azimuthal orders are of special interest. Figure 4(c) shows the electric field intensity surface map of the  $TE_{0,22}$  mode made of pure radial patterns, which exists in an ideal cylindrical cavity of radius  $\rho_c = 17.7 \mu\text{m}$ . This mode exhibits an important concentration of light in the center of the cavity, which can be quantified with the mode surface  $S$  defined as

$$S = \frac{\int \epsilon E^2(r) d^2 r}{\epsilon E_{max}^2}. \quad (2)$$

For the  $TE_{0,22}$  mode, we obtain  $S \sim 12\lambda^2$  ( $\lambda = 1.5 \mu\text{m}$ ), which represents around 3% of the cylinder section ( $\sim 437\lambda^2$ ). In other words, most of the electric energy of the mode is contained in a disk of radius  $\rho \simeq 2.9 \mu\text{m}$ , which covers the first three maxima of the intensity profile.

### B. Finite-difference time-domain (FDTD) simulations

In addition to analytic predictions, we performed FDTD simulations (*LUMERICAL*) based on a more realistic model: we computed the optical response of the microtube with the structured membrane. The model now takes into account the reflectivity of the real rolled-up PCM. We simulated the spectral response of the photonic microtube to a dipolar excitation and extracted quality factors of the detected modes. The modeled structure consists in a rolled-up PCM of thickness  $0.230 \mu\text{m}$ , inner radius  $\rho_{in} = 17.62 \mu\text{m}$  (close to radii of fabricated structures), and the following photonic crystal lattice parameters:  $a = 1.206 \mu\text{m}$ ,  $r = 0.480 \mu\text{m}$ . To excite all the possible modes, we used several electric dipoles randomly positioned inside the microtube and oriented along one diameter. We recorded the

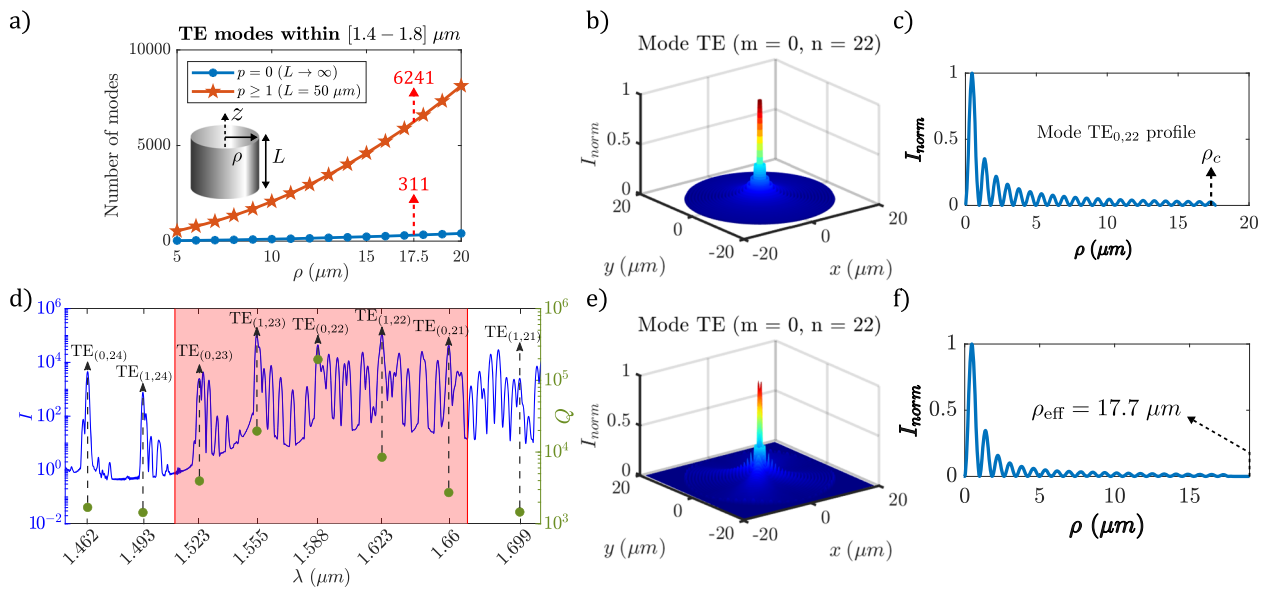


**FIG. 4.** Analytic model of the cylindrical cavity resonator with radius  $\rho$  [plots (a)–(c)]. (a) Number of TE modes within the spectral range [1.4–1.8]  $\mu\text{m}$  as a function of the cavity radius  $\rho$  and for a given height  $L$  of the cavity (inset); (b) surface map and (c) profile of the electric intensity of mode  $\text{TE}_{0,22}$  in the cross section of the cavity of radius  $\rho_c = 17.7 \mu\text{m}$  at  $1.589 \mu\text{m}$ . FDTD simulations of the optical response of a photonic tube with radius  $\rho \approx 17.6 \mu\text{m}$ , membrane width  $h = 0.228 \mu\text{m}$ , and infinite length  $L$  [(plots (d)–(f)]. (d) Intensity spectrum of the photonic microtube excited by multiple electric dipoles positioned in the center of the tube and oriented along one diameter; TE modes with low azimuthal orders and their quality factors  $Q$  (green dots) are also indicated; the high reflectivity zone ( $R > 95\%$ ) of the planar PCM at normal incidence is delimited by the red patch; (e) electric field intensity surface map of mode  $\text{TE}_{0,22}$  simulated in the section of the tube at  $1.588 \mu\text{m}$ ; (f) profile along one radius of the tube of mode  $\text{TE}_{0,22}$ .

temporal response at different points dispersed inside the photonic microtube. We finally Fourier transformed the time data to get the spectral response of the microtube. Due to the multi-scale nature of the structure, we conducted computations on an infinitely long microtube to achieve reasonable simulation times. In this particular case, only TE modes with null axial order  $p$  (infinite spatial extension along the tube axis) can be excited.

Figure 4(d) presents the resulting spectral response of the photonic microtube. In order to identify the nature of the obtained modes, we calculated the distribution of the electric intensity in the section of the microtube. Figure 4(e) shows the electric intensity surface map of the mode detected at  $1.588 \mu\text{m}$ . The pure radial patterns observed are typical of cylindrical cavity modes with a low azimuthal order. The analysis of the intensity maps of the other modes revealed that they all correspond to cylindrical cavity modes  $\text{TE}_{m,n}$  consistently with previous analytical predictions. The determination of the orders of the modes is performed by extracting a profile along one diameter of the microtube and by comparing it to analytical profiles in an ideal cylindrical cavity of radius  $\rho$ . One profile of the mode detected at  $1.588 \mu\text{m}$  is displayed in Fig. 4(f): it matches with the analytical profile of the  $\text{TE}_{0,22}$  mode for an effective cavity radius  $\rho_{\text{eff}} = 17.68 \mu\text{m}$ . The radius  $\rho_{\text{eff}}$  corresponds to the radius of an equivalent ideal cylindrical cavity with infinitely thin and perfectly reflecting walls. The difference between  $\rho_{\text{eff}}$  and the real radius of the microtube reaches  $0 \mu\text{m}, 06 \mu\text{m}$ : it represents the penetration length of the mode in the membrane walls.

Also in agreement with analytical results for a microtube of infinite length, a high number of TE modes are excited in the spectral range from  $1.4 \mu\text{m}$  to  $1.8 \mu\text{m}$ . In Fig. 4(d), we can notice a

repeated pattern in the spectral distribution of the modes, in which one principal mode is accompanied by secondary modes with spacing increasing with the wavelength. The identification of the modes' orders demonstrates that the principal modes correspond to  $\text{TE}_{m,n}$  modes with low azimuthal orders  $m = \{0, 1\}$  as indicated on the spectrum, whereas secondary peaks relate to modes with higher azimuthal orders  $m \geq 2$ . Low azimuthal modes are of special interest because of their ability to concentrate light in the center of the microtube, as demonstrated in Sec. IV A, for mode  $\text{TE}_{0,22}$ . The correspondence between the wavelength at which those modes are detected,  $\lambda_{\text{FDTD}}$ , and the analytical cutoff wavelengths is excellent with a relative error on the order of 0.1% for an effective radius  $\rho_{\text{eff}} = 17.68 \mu\text{m}$ , as presented in Table I. To assess the impact of the reflectivity on low azimuthal modes' quality factors  $Q$ , we computed them separately using single dipole excitation to isolate the modes of interest. The results are presented in Fig. 4(a) (green dots) and shown as expected:  $Q$  is maximum when the reflectivity is maximum. Hence, the quality factor of mode  $\text{TE}_{0,22}$  reaches the highest value  $Q = 10^5$  at  $1.588 \mu\text{m}$ , which corresponds indeed to the maximum of reflectivity of the planar PCM at normal incidence. These results reveal two important features for the photonic microtube: first, TE modes with low azimuthal orders can be excited in the photonic microtube and maintained in the cavity, considering the high  $Q$  values in the high reflectivity region of the planar PCM. Second, the reflectivity of the planar PCM seems not to be affected by the curvature as expected in previous design considerations ( $\rho \gg a$ ).

Finally, the estimation of the mode surface of the  $\text{TE}_{0,22}$  mode simulated with FDTD simulations gives  $S \sim 12\lambda^2$ , namely, around

**TABLE I.** Wavelengths of the  $TE_{m,n}$  modes obtained by 2D FDTD simulations  $\lambda_{\text{FDTD}}$  compared with analytical solutions  $\lambda_{\text{th}}$  with the effective radius of the microtube  $\rho_{\text{eff}} = 17.68 \mu\text{m}$ ;  $R$  is the reflectivity of the planar membrane at normal incidence.

$TE_{(m,n)}$	$R$ (%)	$\lambda_{\text{FDTD}}$	$\lambda_{\text{th}}$	Relative error (%)
(0, 24)	83.5	1.4625	1.4582	0.82
(1, 24)	90.9	1.4925	1.4891	0.23
(0, 23)	96.2	1.5228	1.5210	0.12
(1, 23)	99.1	1.5549	1.5546	0.02
(0, 22)	99.9	1.5881	1.5893	0.08
(1, 22)	98.8	1.6232	1.6261	0.17
(0, 21)	95.8	1.6598	1.6641	0.26
(1, 21)	92.7	1.6986	1.7044	0.34

3% of the cavity cross section ( $436\lambda^2$ ), which is in perfect agreement with analytic results.

## V. OPTICAL CHARACTERIZATION OF PHOTONIC MICROTUBES

### A. Experimental setup

Fabricated photonic microtubes were optically characterized. As cavity modes are strongly confined inside the structure, an efficient way to excite those modes is to place an emitter or a dipole directly inside the cavity, as sketched in Fig. 5(a). To achieve this goal, we used a custom-designed SNOM equipped with an optical bowtie nano-antenna (NA), as shown in Fig. 5(b), operating in the near-infrared range. Indeed, resonant nano-antennas and especially bowtie nano-apertures (BNAs) are good candidates for our application for several reasons. First, they present a strong enhancement of the electric field inside the air gap, which insures a dramatic light-matter interaction at the nanoscale. Second, the optical capacitive effect in the gap induces an electric dipole, which interacts mainly with a single component of the electric field, perpendicularly to the gap.<sup>26</sup> Previous works showed that the BNA integrated at the apex of an optical fiber tip acted as a high-resolution polarizing nano-collector and can be used as a very efficient nanopolarizer.<sup>27</sup> In this work, we introduced a similar BNA near-field

probe inside the microtube of length  $L$  and radius  $\rho$  at a penetration depth  $d$ , as defined in Fig. 5(b). To excite the cylindrical cavity modes, light is injected inside the optical fiber to the BNA probe. The signal re-emitted by the nano-antenna is collected by the optical fiber again to a detector, as depicted in Fig. 5(b). Its intensity is directly related to the electromagnetic environment of the probe, which is governed by the resonant modes. The incident light is provided by a tunable TUNICS laser source, which covers a spectral range from  $1.450 \mu\text{m}$  to  $1.580 \mu\text{m}$  with a minimal spectral increment of  $0.1 \text{ nm}$ . A fiber splitter enables to separate the incoming (light excitation) and the outgoing (the collected light) signals with a signal ratio of 10/90. In this illumination-collection configuration, the probe is scanned horizontally along a section of the tube to obtain the electric field intensity maps of the modes. Figure 5(c) presents one typical intensity map obtained after a scan of the top of the photonic microtube. The azimuthal patterns coming from the structure serve as guides to approach and center the probe in relation to the microtube [dashed black outline in Fig. 5(c)].

### B. Results and discussion

SNOM measurements were carried out on a  $50 \mu\text{m}$ -long photonic microtube with a radius of about  $17.5 \mu\text{m}$  and a  $0.230 \mu\text{m}$ -thick membrane wall. Due to the size of the taper, the vertical introduction of the probe inside the tube, namely, the penetration depth  $d$ , imposes a limit to the maximum scan area, as presented in Fig. 6(a).

Our results showed that a mode pattern could be obtained for every wavelength, which is in agreement with the predicted high density of modes. In particular, Fig. 6(a) shows a typical mode pattern detected at the excitation wavelength  $\lambda_1 = 1.450 \mu\text{m}$ . For this mode, the electric field intensity pattern shows concentric circles with a minimum, or node, in the center of the cavity. Note that due to the polarizing effect of the nano-antenna, the contrast of these radial oscillations is essentially visible in one direction. It gives an experimental indication of the orientation of the BNA as represented by the dashed yellow contour in Fig. 6(a). This radial pattern is typical of cylindrical cavity modes characterized by low azimuthal orders. To determine the mode order, the experimental profile of the mode was compared to the analytical profile. The

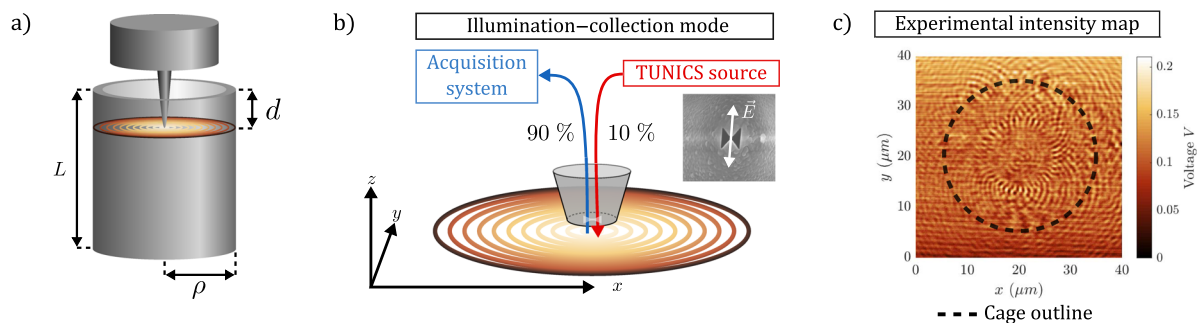


**FIG. 5.** Schematic overview of a SNOM measurement: (a) the probe is plunged into the cylindrical cavity of radius  $\rho$  and length  $L$  at a penetration depth  $d$ ; (b) illumination-collection mode: a tunable TUNICS laser source provides a light signal into the fiber terminated by a bowtie nano-aperture (BNA), which radiates the light signal into the photonic microtube and collects its response; (c) typical electric intensity map obtained at the top of the microtube ( $d \approx 0 \mu\text{m}$ ).



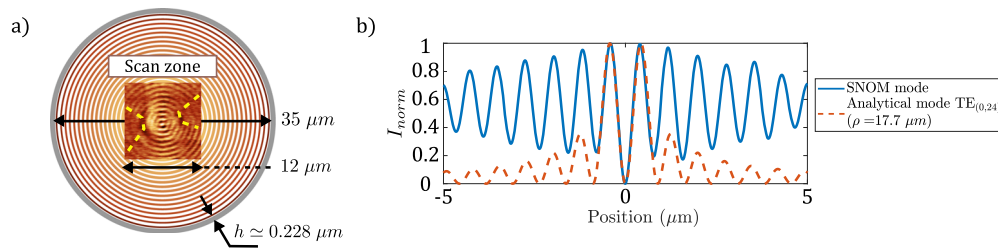


**FIG. 6.** (a) Experimental map of the electric field intensity obtained at  $\lambda_1 = 1.450 \mu\text{m}$ . The BNA is introduced inside the  $50 \mu\text{m}$ -long photonic microtube (diameter of  $35 \mu\text{m}$ ) at a penetration depth  $d \approx 15 \mu\text{m}$ . The scan picture is included in a scale drawing of the photonic microtube cross section, and the detected mode is schematically extended until the membrane wall. The dashed yellow contour highlights polarizing effects of the BNA. (b) Comparison between one filtered profile of the experimental mode along one diameter of the microtube and the analytical profile of mode  $\text{TE}_{0,24}$  for  $\rho_{\text{eff}} = 17.7 \mu\text{m}$ .

original scan picture is filtered beforehand to remove high spatial frequency noise and preserve only the information on the spatial oscillations of the mode. Therefore, Fig. 6(b) shows that the positions of the intensity maxima in the filtered profile of the mode (straight blue curve) match with those in the analytical profile of the  $\text{TE}_{0,24}$  mode (dashed orange curve) for an effective cavity radius  $\rho_{\text{eff}} = 17.7 \mu\text{m}$ . The wavelength of detection of mode  $\text{TE}_{0,24}$ ,  $\lambda_1 = 1.450 \mu\text{m}$ , is consistent with its wavelength of appearance in FDTD simulations (see Sec. IV B),  $\lambda = 1.462 \mu\text{m}$ , for a similar effective radius of cavity. The observation of cavity modes inside a real photonic microtube validates the 2D numerical predictions obtained with the FDTD method. It also brings the experimental proof of concept of photon cages in the case of the rolled-up 2D PCM.

Other scans were performed while varying the excitation wavelength from  $1.450 \mu\text{m}$  to  $1.580 \mu\text{m}$ . Figure 7(a) presents three intensity maps recorded at  $\lambda_2 = 1.480 \mu\text{m}$ ,  $\lambda_3 = 1.510 \mu\text{m}$ , and  $\lambda_4 = 1.540 \mu\text{m}$ . In each case, we observe cylindrical cavity modes and especially TE modes with low azimuthal orders, namely,  $m = 0$  and  $m = 1$ , characterized by a minimum and a maximum of the intensity, respectively, in the center of the map. At first sight, both intensity patterns obtained at  $\lambda_2$  and  $\lambda_4$  seem to have identical radial oscillations. However, when we compare the associated profiles extracted along one radius of the tube in Fig. 7(b), it is clear by the apparent shift that both modes have different radial orders. This is confirmed by the determination of the orders of the modes using the analytical model: modes at  $\lambda_2$  and  $\lambda_4$  correspond to  $\text{TE}_{1,24}$  and  $\text{TE}_{1,23}$  modes,

respectively. In the same way, the mode detected at  $\lambda_3$  matches with the  $\text{TE}_{0,23}$  mode.

It is noteworthy that we only detect pure radial patterns characterized by low azimuthal orders. Two reasons can explain this specific sensitivity. First, azimuthal patterns form when light rays hit the membrane walls of the photonic microtube at oblique incidence. Therefore, the existence of a mode with a high azimuthal order, arising for a given angle of incidence  $\theta$ , crucially depends on the reflection power of the membrane at the angle  $\theta$ . In the operation range of the TUNICS laser source,  $[1, 45-1, 580] \mu\text{m}$ , the reflectivity of the planar PCM severely deteriorates with the increasing angle of incidence according to Fig. 2, while it remains at a high value at normal incidence. Hence, modes with high azimuthal orders are hardly excited or not. Second, as mentioned previously, the size of the scanning area is limited by the size of the taper so that the BNA detects preferentially modes with low azimuthal orders. Indeed, when the azimuthal order increases for a given radial order, azimuthal patterns get closer to the membrane walls and the central intensity node widens so that the mode comes out of the scanning zone.

Furthermore, the spectral evolution of the experimental modes agrees with analytic and numerical predictions. We alternately detect  $\text{TE}_{m,n}$  modes with  $m = 0$  and  $m = 1$  and radial order  $n$  decreasing with the excitation wavelength. However, from one mode to another, we always observe radial patterns when we gradually increase the excitation wavelength. In fact, the photonic microtube has a finite length  $L$ , and light is also reflected at its upper and

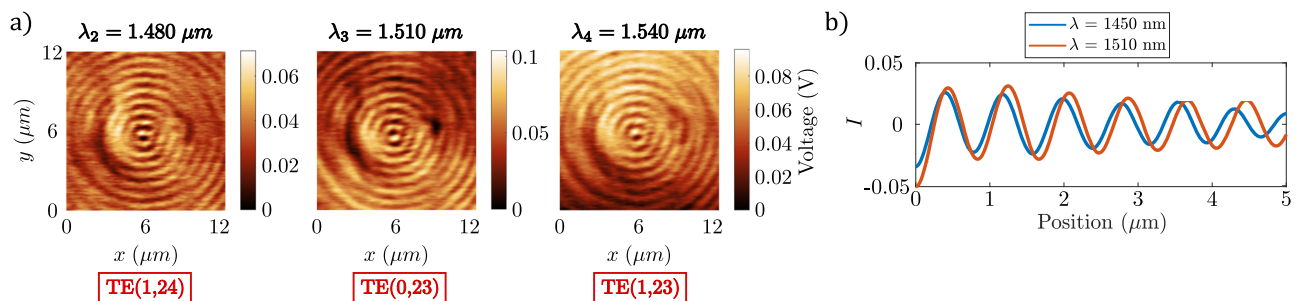


**FIG. 7.** (a) Experimental maps of the electric field intensity obtained at three distinct excitation wavelengths  $\lambda_2 = 1.480 \mu\text{m}$ ,  $\lambda_3 = 1.510 \mu\text{m}$ , and  $\lambda_4 = 1.540 \mu\text{m}$  with their associated orders  $(m, n)$ . (b) Comparison between experimental profiles of modes obtained at  $\lambda_2$  and  $\lambda_4$ .

lower boundaries on account of the impedance mismatch between the inside and the outside of the microtube. This implies the quantization of the projection of the light wavevector along the microtube axis, as announced in Sec. IV A:  $k_z = p\pi/L$ , where  $p \in \mathbb{N}^*$  is the axial order. For a given couple  $(m, n)$ , the value of  $p$  determines the intensity profile along the tube axis. Therefore, between two successive modes  $TE_{0,n,1}$  and  $TE_{1,n,1}$ ,  $TE_{1,n,p}$  modes with  $p > 1$  exist and exhibit the same intensity distribution in the section of the microtube as the fundamental mode  $TE_{1,n,1}$ . This is represented in Fig. 8, which plots the evolution of the cutoff wavelengths of modes  $TE_{0,24,p}$  (stars),  $TE_{1,24,p}$  (squares),  $TE_{0,23,p}$  (triangles), and  $TE_{1,23,p}$  (circles) with  $p$  (namely,  $k_z$ ) varying from 0 (case of an infinitely long microtube) to 10 for a photonic microtube of effective radius  $\rho_{\text{eff}} = 17.7 \mu\text{m}$  and length  $L = 50 \mu\text{m}$ . For instance, between fundamental modes  $TE_{0,24,1}$  and  $TE_{1,24,1}$ , we can detect  $TE_{1,24,p}$  modes with  $p = 2, 3, \dots, 14$ , which will exhibit the same electric field intensity distribution in the section of the microtube as for the  $TE_{1,24,1}$  mode. Wavelengths  $\lambda_1, \lambda_2, \lambda_3$ , and  $\lambda_4$  correspond to the wavelengths at which we detect experimentally the modes presented in Figs. 6(a) and 7(a). According to the dispersion, modes at  $\lambda_1, \lambda_2, \lambda_3$  have associated  $p$  orders of 8 and 9 for the mode at  $\lambda_4$ . Moreover, the spacing between the first two adjacent modes  $TE_{1,24,1}$  and  $TE_{1,24,2}$  is estimated to be 0.5 nm. Probably due to the spectral overlapping between the modes, the transition between those two modes with different axial orders is not appreciable on the intensity maps. It is important to note that the determination of orders  $p$  of the modes as well as their quality factors  $Q$  would represent a valuable hint to justify this behavior. Additional near-field measurements have been carried out on 50  $\mu\text{m}$ -long photonic microtubes with a smaller radius  $\rho \approx 15 \mu\text{m}$ . The probe was driven down the tube at  $d \approx 8 \mu\text{m}$ . Cylindrical cavity modes with low azimuthal orders are again recorded, and their orders were determined with the analytic model. For a smaller tube, we expect a decrease in the radial order of a mode at a fixed wavelength. This is indeed confirmed experimentally: at 1.580  $\mu\text{m}$ , we detect the  $TE_{0,19,p}$  mode, whereas at the same excitation wavelength but for the 17.5  $\mu\text{m}$ -radius microtube, the mode corresponds to the  $TE_{0,22,p}$  mode. Those results also

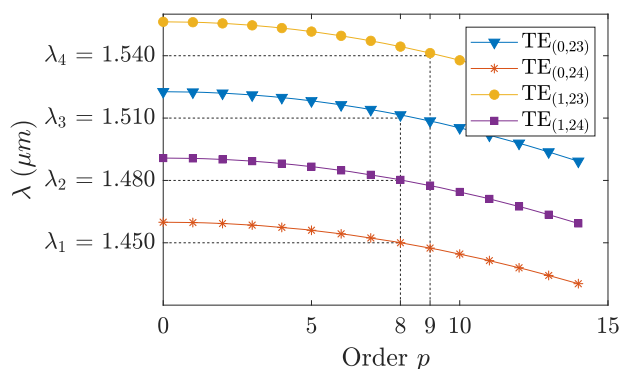


**FIG. 8.** Analytic dispersion of modes  $TE_{0,24}$ ,  $TE_{1,24}$ ,  $TE_{0,23}$ , and  $TE_{1,23}$  where  $p \in \mathbb{N}^*$  is the axial order for a photonic microtube of effective radius  $\rho = 17.7 \mu\text{m}$  and length  $L = 50 \mu\text{m}$ . Wavelengths  $\lambda_1, \lambda_2, \lambda_3$ , and  $\lambda_4$  correspond to the excitation wavelengths at which the modes are detected in SNOM measurements.

prove the reproducibility of the SNOM measurements with the current setup. In addition, the consistency of the photon cage concept is reinforced, and the quality of the fabricated structures is guaranteed.

## VI. CONCLUSION AND PERSPECTIVES

This work has brought the proof of concept of photon cages based on rolled-up 2D photonic crystal membrane (PCM) mirrors in the near-infrared domain. We showed that, as expected, such structures can confine light in air and in the center of the cavity. Indeed, matching analytical and FDTD computations confirmed that the cages so formed behave as cylindrical resonators with perfectly reflecting membrane walls. In particular, they revealed the presence of radial modes that concentrate most of the electric field intensity in the center of the cavity, over about 3% of the cavity cross-sectional area, and present high quality factors up to  $10^5$ . We demonstrated that the stress-engineering fabrication technique was efficient to roll the 2D PCM into 3D hollow micro-resonators. We reported therefore the successful fabrication of tubular photon cages made of an InP/InGaP pre-stressed bilayer with a precise control on geometrical parameters. Finally, we demonstrated experimentally that optical modes could be sustained in air in the center of photonic cylindrical cavities. A customized scanning near-field optical microscope (SNOM) was used to probe the cavity modes in the hollow part of the tubular cages with a polarization-selective bowtie nano-antenna. The electric field intensity maps of TE cavity modes extracted in the center of the cavity showed mainly pure radial patterns, in very good agreement with theoretical and numerical computations. Those promising results open new perspectives in the study of the optical behavior of such photonic microtubes. It is noteworthy that due to the size of the cavities, the high density of modes makes the experimental determination of the quality factors of the modes delicate. However, the introduction of a real emitter inside the tube by using active probes, for instance, would help get the spectral signature of the cylindrical cavity modes and assess their quality factors. The ability of those microstructures to confine light efficiently in air makes their use possible for opto-fluidic operations such as fluid sensing. The successful combination of a highly reflecting PCM and stress engineering provides a promising step for the creation of 3D photonic microstructures. Indeed, it opens the path for 3D micro-objects with customizable photonic functionalities, considering the variety of possible 3D geometries and the versatile use of photonic crystals, enriching the existing assortment of non-structured 3D photonic micro-objects.

## ACKNOWLEDGMENTS

This work was funded by PHOLDING Project No. ANR-17-CE24-0027. The authors thank the Nanolyon technological and experimental platform for assistance during the development of this study. We thank PMCS2I of Ecole Centrale de Lyon for allowing us to use Newton computer cluster facilities to perform the FDTD simulations. We are also indebted to J.-Y. Rauch for support in the fabrication of the BNAs. The nanoantennas integrated on fiber tips were fabricated at MIMENTO and IEMN technology platforms in the framework of the NANOEC project, Grant No. ANR07-NANO-036.

## DATA AVAILABILITY

The data that support the findings of this study are available from the corresponding author upon reasonable request.

## REFERENCES

- <sup>1</sup>V. Y. Prinz, V. A. Seleznev, A. K. Gutakovskiy, A. V. Chehovskiy, V. V. Preobrazhenskii, M. A. Putyato, and T. A. Gavrilova, "Free-standing and overgrown InGaAs/GaAs nanotubes, nanohelices and their arrays," *Physica E* **6**, 828–831 (2000).
- <sup>2</sup>V. Y. Prinz, D. Grützmacher, A. Beyer, C. David, B. Ketterer, and E. Deckardt, "A new technique for fabricating three-dimensional micro- and nanostructures of various shapes," *Nanotechnology* **12**, 399 (2001).
- <sup>3</sup>O. G. Schmidt and K. Eberl, "Nanotechnology: Thin solid films roll up into nanotubes," *Nature* **410**, 168 (2001).
- <sup>4</sup>M. Huang, C. Boone, M. Roberts, D. E. Savage, M. G. Lagally, N. Shaji, H. Qin, R. Blick, J. A. Nairn, and F. Liu, "Nanomechanical architecture of strained bilayer thin films: From design principles to experimental fabrication," *Adv. Mater.* **17**, 2860–2864 (2005).
- <sup>5</sup>J. Zanardi Ocampo, P. O. Vaccaro, K. Kubota, T. Fleischmann, T.-S. Wang, T. Aida, T. Ohnishi, A. Sugimura, R. Izumoto, M. Hosoda, and S. Nashima, "Characterization of GaAs-based micro-origami mirrors by optical actuation," *Microelectron. Eng.* **73–74**, 429–434 (2004).
- <sup>6</sup>A. Danescu, C. Chevalier, G. Grenet, P. Regreny, X. Letartre, and J. L. Leclercq, "Spherical curves design for micro-origami using intrinsic stress relaxation," *Appl. Phys. Lett.* **102**, 123111 (2013).
- <sup>7</sup>F. Cavallo and M. G. Lagally, "Nano-origami: Art and function," *Nano Today* **10**, 538–541 (2015).
- <sup>8</sup>A. Danescu, P. Regreny, P. Cremillieu, and J.-L. Leclercq, "Fabrication of self-rolling geodesic objects and photonic crystal tubes," *Nanotechnology* **29**, 285301 (2018).
- <sup>9</sup>J.-H. Cho, M. D. Keung, N. Verellen, L. Lagae, V. V. Moshchalkov, P. Van Dorpe, and D. H. Gracias, "Nanoscale origami for 3D optics," *Small* **7**, 1943–1948 (2011).
- <sup>10</sup>H. J. In, S. Kumar, Y. Shao-Horn, and G. Barbastathis, "Origami fabrication of nanostructured, three-dimensional devices: Electrochemical capacitors with carbon electrodes," *Appl. Phys. Lett.* **88**, 083104 (2006).
- <sup>11</sup>B. Xu, B. Zhang, L. Wang, G. Huang, and Y. Mei, "Tubular micro/nanomachines: From the basics to recent advances," *Adv. Funct. Mater.* **28**, 1705872 (2018).
- <sup>12</sup>X. Guo, H. Li, B. Yeop Ahn, E. B. Duoss, K. J. Hsia, J. A. Lewis, and R. G. Nuzzo, "Two- and three-dimensional folding of thin film single-crystalline silicon for photovoltaic power applications," *Proc. Natl. Acad. Sci. U. S. A.* **106**, 20149–20154 (2009).
- <sup>13</sup>M. Yu, Y. Huang, J. Ballweg, H. Shin, M. Huang, D. E. Savage, M. G. Lagally, E. W. Dent, R. H. Blick, and J. C. Williams, "Semiconductor nanomembrane tubes: Three-dimensional confinement for controlled neurite outgrowth," *ACS Nano* **5**, 2447–2457 (2011).
- <sup>14</sup>S. M. Harazim, V. A. Bolaños Quiñones, S. Kiravittaya, S. Sanchez, and O. G. Schmidt, "Lab-in-a-tube: On-chip integration of glass optofluidic ring resonators for label-free sensing applications," *Lab Chip* **12**, 2649–2655 (2012).
- <sup>15</sup>Y. Li, Y. Fang, J. Wang, L. Wang, S. Tang, C. Jiang, L. Zheng, and Y. Mei, "Integrative optofluidic microcavity with tubular channels and coupled waveguides via two-photon polymerization," *Lab Chip* **16**, 4406–4414 (2016).
- <sup>16</sup>A. Madani, S. M. Harazim, V. A. Bolaños Quiñones, M. Kleinert, A. Finn, E. S. Ghareh Naz, L. Ma, and O. G. Schmidt, "Optical microtube cavities monolithically integrated on photonic chips for optofluidic sensing," *Opt. Lett.* **42**, 486–489 (2017).
- <sup>17</sup>F. Li and Z. Mi, "Optically pumped rolled-up InGaAs/GaAs quantum dot microtube lasers," *Opt. Express* **17**, 19933 (2009).
- <sup>18</sup>Y. Li, L. Feng, X. Su, Q. Li, F. Yun, G. Yuan, and J. Han, "Whispering gallery mode lasing from InGaN/GaN quantum well microtube," *Opt. Express* **25**, 18072–18080 (2017).
- <sup>19</sup>M. R. Jorgensen, S. Giudicatti, and O. G. Schmidt, "Diamond lattice photonic crystals from rolled-up membranes," *Phys. Rev. A* **87**, 041803 (2013).
- <sup>20</sup>H. T. Hattori, X. Letartre, C. Seassal, P. Rojo-Romeo, J.-L. Leclercq, and P. Viktorovitch, "Analysis of hybrid photonic crystal vertical cavity surface emitting lasers," *Opt. Express* **11**, 1799–1808 (2003).
- <sup>21</sup>W. Suh, M. F. Yanik, O. Solgaard, and S. Fan, "Displacement-sensitive photonic crystal structures based on guided resonance in photonic crystal slabs," *Appl. Phys. Lett.* **82**, 1999–2001 (2003).
- <sup>22</sup>S. Boutami, B. Benbakir, X. Letartre, J. L. Leclercq, P. Regreny, and P. Viktorovitch, "Ultimate vertical Fabry-Perot cavity based on single-layer photonic crystal mirrors," *Opt. Express* **15**, 12443 (2007).
- <sup>23</sup>X. Letartre, J. Mouette, J. L. Leclercq, P. R. Romeo, C. Seassal, and P. Viktorovitch, "Switching devices with spatial and spectral resolution combining photonic crystal and MOEMS structures," *J. Lightwave Technol.* **21**, 1691 (2003).
- <sup>24</sup>C. Sieutat, R. Peretti, J.-L. Leclercq, P. Viktorovitch, and X. Letartre, "Strong confinement of light in low index materials: The photon cage," *Opt. Express* **21**, 20015–20022 (2013).
- <sup>25</sup>D. M. Pozar, *Microwave Engineering*, 4th ed. (Wiley, Hoboken, NJ, 2011).
- <sup>26</sup>M. Mivelle, I. A. Ibrahim, F. Baida, G. W. Burr, D. Nedeljkovic, D. Charrat, J.-Y. Rauch, R. Salut, and T. Grosjean, "Bowtie nano-aperture as interface between near-fields and a single-mode fiber," *Opt. Express* **18**, 15964–15974 (2010).
- <sup>27</sup>T.-P. Vo, M. Mivelle, S. Callard, A. Rahmani, F. Baida, D. Charrat, A. Belarouci, D. Nedeljkovic, C. Seassal, G. W. Burr, and T. Grosjean, "Near-field probing of slow Bloch modes on photonic crystals with a nanoantenna," *Opt. Express* **20**, 4124 (2012).
- <sup>28</sup>E. Saei Ghareh Naz, M. R. Jorgensen, and O. G. Schmidt, "Density of optical states in rolled-up photonic crystals and quasi crystals," *Comput. Phys. Commun.* **214**, 117–127 (2017).